- Quantifying Force Transmission through Fibroblasts:
- Changes of Traction Forces under External Shearing

- **Steven Huth¹, Johannes W. Blumberg², Dimitri Probst², Jan Lammerding³, Ulrich S.**
- ⁴ Schwarz^{2,*}, and Christine Selhuber-Unkel^{4,*}
- ⁵ Institute of Materials Science, Biocompatible Nanomaterials, Kiel University, Kaiserstr. 2, D-24143 Kiel, Germany
- 6 ²Institute for Theoretical Physics and Bioquant-Center for Quantitative Biology, Heidelberg University,
- Philosophenweg 19, D-69120 Heidelberg, Germany
- ⁸ Weill Institute for Cell and Molecular Biology and Meinig School of Biomedical Engineering, Cornell University, 235
- 9 Weill Hall, Ithaca, NY 14853, USA
- ⁴Institute for Molecular Systems Engineering (IMSE), Heidelberg University, INF 253, D-69120, Heidelberg,
- 11 Germany
- *schwarz@thphys.uni-heidelberg.de, selhuber@uni-heidelberg.de

Mammalian cells have evolved complex mechanical connections to their microenvironment, including focal adhesion clusters that physically connect the cytoskeleton and the extracellular matrix. This mechanical link is also part of the cellular machinery to transduce, sense and respond to external forces. Although methods to measure cell attachment and cellular traction forces are well-established, these are not capable of quantifying force transmission through the cell body to adhesion sites. We here present a novel approach to quantify intracellular force transmission by combining microneedle shearing at the apical cell surface with traction force microscopy at the basal cell surface. The change of traction forces exerted by fibroblasts to underlying polyacrylamide substrates as a response to a known shear force exerted with a calibrated microneedle reveals that cells redistribute forces dynamically under external shearing and during sequential rupture of their adhesion sites. Our quantitative results demonstrate a transition from dipolar to monopolar traction patterns, an inhomogeneous distribution of the external shear force to the adhesion sites as well as dynamical changes in force loading prior to and after the rupture of single adhesion sites. Our strategy of combining traction force microscopy with external force application opens new perspectives for future studies of force transmission and mechanotransduction in cells.

5 Introduction

Cells exert forces to interact with their surroundings and have the striking ability to react to externally applied forces and mechanical cues by a process called mechanotransduction^{1–3}. Cellular reactions to external mechanical cues play a crucial role in cellular processes such as stem cell differentiation, adhesion, migration, and proliferation^{4–8}. Furthermore, focal adhesion clusters grow in response to external shearing^{9,10} which might help cells to withstand shear forces, e.g. forces exerted by the blood flow on endothelial cells^{11,12}.

Traction force microscopy (TFM) has become an established tool to quantify forces exerted by single cells or cell layers to the underlying substrate, which has deepened our understanding of cell migration, mechanotransduction and cell-matrix interaction 13–20. However, current traction force microscopy models assume an equilibrium of a cell's traction forces, whereas in nature cells experience a variety of externally applied forces, for instance from blood flow, muscle contraction, movement of other cells, or wound

opening. Force transmission is particularly important in tissue formation and adaption²¹ as well as in collective cell migration, where many cells interact with each other and mechanically strong cells become leader cells^{19,22}. Thus, to understand force transmission by cells more completely, it is crucial to study traction forces under external forces.

Techniques to exert mechanical stimuli to cells include atomic force microscopy (AFM), which can be employed to measure forces necessary to rupture cellular adhesions^{23,24} or forces exerted by cells^{25,26}, hydrodynamic shear stress^{11,12,27}, optical or magnetic tweezers^{3,28–30}, microneedle assays^{9,10,31} and optical stretchers^{32,33}. Despite the fact that such a large variety of physical cell manipulation techniques has been established and cellular forces exerted to surfaces can be measured via TFM or elastic resonator interference stress microscopy¹⁶, a quantification of cellular force adaptation as a response to well-defined mechanical stimuli applied to cells has not yet been realized.

Here, we present a new tool that combines TFM with externally applied mechanical stimulation by microneedle shearing. This setting allows to quantify cellular force transmission by measuring how cells distribute an external well-defined shear force to their adhesion sites. The spring constant of the microneedle is calibrated and thus the shear force exerted by the needle is known. We advanced current TFM procedures to create a novel procedure that analyzes traction forces in the presence of an external force monopole. This new force transmission assay is a versatile technique that is complementary to existing methods, as it can also be combined with other techniques such as AFM to broaden our understanding of the interplay of cellular biomechanics and adhesion.

46 Results and Discussion

To investigate the force transmission from the apical to the basal side of an adherent cell, we conducted
experiments during which we exerted well-defined shear forces to the apical side of mouse embryonic
fibroblasts (MEFs) while simultaneously measuring the change in traction forces at their basal side. We
employed MEF fibroblasts expressing mNeonGreen (NeonG) labeled zyxin as a marker for focal adhesions.
Cells were allowed to spread on a fibronectin-functionalized polyacrylamide (PAAm) gel with embedded
red fluorescent marker beads so that traction forces could be derived from recording the displacement of
the marker beads. A microneedle was installed into a micromanipulator such that the tip of the microneedle

was parallel to the cell substrate. Moving the microneedle with a computer-controlled micromanipulator results in the application of a shear force to the apical cell surface. The spring constant of this microneedle was calibrated by shearing polydimethylsiloxane (PDMS) pillars prior to the cell experiments. To do so, first the Young's modulus of the PDMS sample was measured with an AFM-based indentation method³⁴ 57 (see Supplementary Information). Then, the calibration of the microneedle was carried out by moving a 58 microneedle against a PDMS pillar (Fig. 1) and measuring the associated PDMS pillar and microneedle 59 bending. In A and B, representative phase contrast images of the shearing of a PDMS pillar with a 60 microneedle show the bending of pillar and microneedle due to shear forces. Knowing the geometry as 61 well as the Young's modulus of the pillar, the shear force is calculated from the pillar bending³⁵. C shows 62 a plot of the shear force versus the microneedle bending for each frame of the experiment. The slope of a 63 linear fit to this curve corresponds to the microneedle's spring constant.

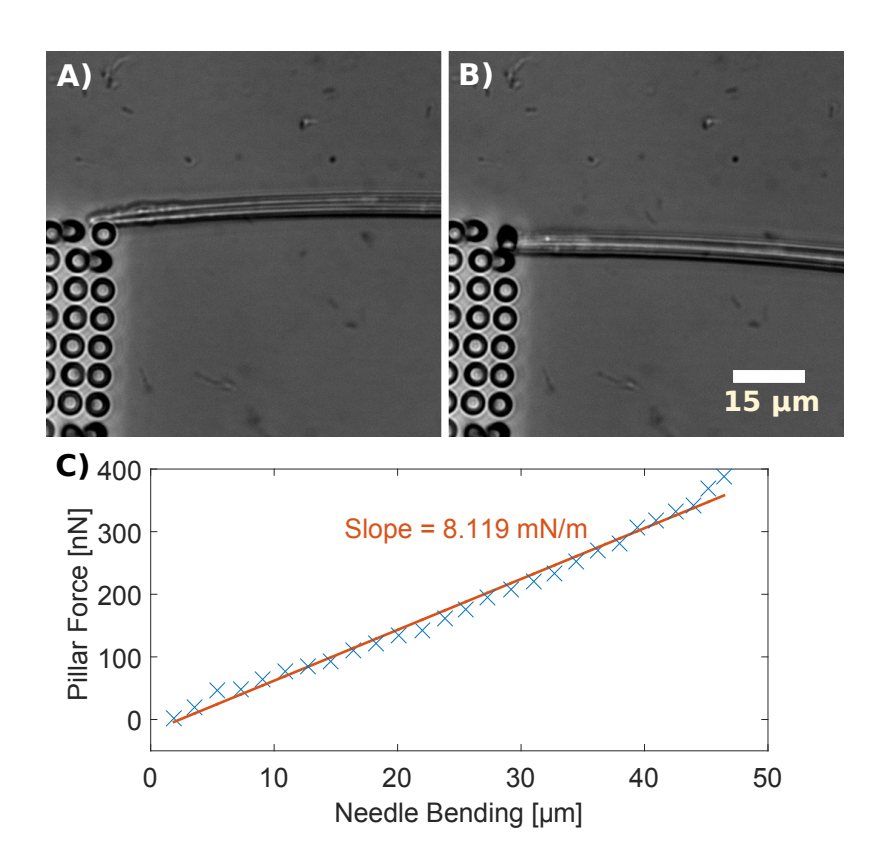


Figure 1. A and **B** show exemplary phase contrast images of a microneedle shearing a PDMS pillar. The needle moves downwards and bends the pillar. The pillar, on the other hand, exerts a force to the needle, which results in a bending of the needle. The force acting between needle and pillar is calculated from the bending of the PDMS pillar. **C** presents a plot of the pillar force versus the bending of the microneedle for each frame of the shearing experiment. The slope corresponds to the microneedle's spring constant.

For the force transmission experiments, the microneedle was carefully inserted into the fibroblast cell 65 directly below or above the nucleus. Subsequently, the microneedle was moved at a constant speed of 5 μm/s towards the nucleus to exert increasing shear forces to the cell until the cell detached from the underlying PAAm substrate. We decided to shear the nucleus, as other modes of exerting shear forces to the cell caused the microneedle to quickly slip away. This is in agreement with published work by Riveline et al.⁹ and Paul et al.¹⁰ who have shown that nucleus shearing is the most efficient way to transmit forces to a cell with a microindenter. During the shearing process, phase contrast images of the cell and needle as well as fluorescent images of the marker beads embedded in the PAAm gel were recorded. Fig. 2 A and B present exemplary phase contrast images of such an experiment. A video containing all phase contrast 73 images as well as another video of the fluorescent marker beads are presented in the Supplementary Information. These phase contrast images were used to monitor the cell as well as to calculate the degree 75 of needle bending for each frame. Knowing the needle's spring constant, the needle bending is a measure 76 for the shear force exerted to the cell. To correlate the measured traction forces with the distribution of 77 adhesion sites, the zyxin distribution of the fibroblast prior to each experiment was recorded (Fig. 2 C). This information is essential, as focal adhesions are the main site of traction force exertion ^{17,18}.

The images of the fluorescent marker beads embedded in the PAAm sample to which the cell is 80 adhering were used as the basis for computing the traction forces that the cell exerted to the PAAm sample 81 as a function of external shear force. As the microneedle applies external shear forces to the cell surface, 82 cellular traction forces are no longer balanced by internal forces only, and the overall force balance has to 83 include the overall force applied by the microneedle. In other words, the cell traction is not dominated by the force dipole contribution, as it is usually the case, but also includes a force monopole. Our experimental setup therefore requires several modifications to the force reconstruction algorithms commonly used in TFM^{15,36}. Due to the existence of a force monopole, deformation is very long-ranged and boundary effects 87 must be considered. In Fourier space, the k=0 mode becomes relevant, which cannot be reconstructed with the standard Fourier Transform Traction Cytometry (FTTC) procedures due to the divergence of the Green's function at k = 0. Finally, TFM usually uses the inverse method which requires regularization, but this procedure tends to underestimate absolute force values, which are especially important in our context³⁶.

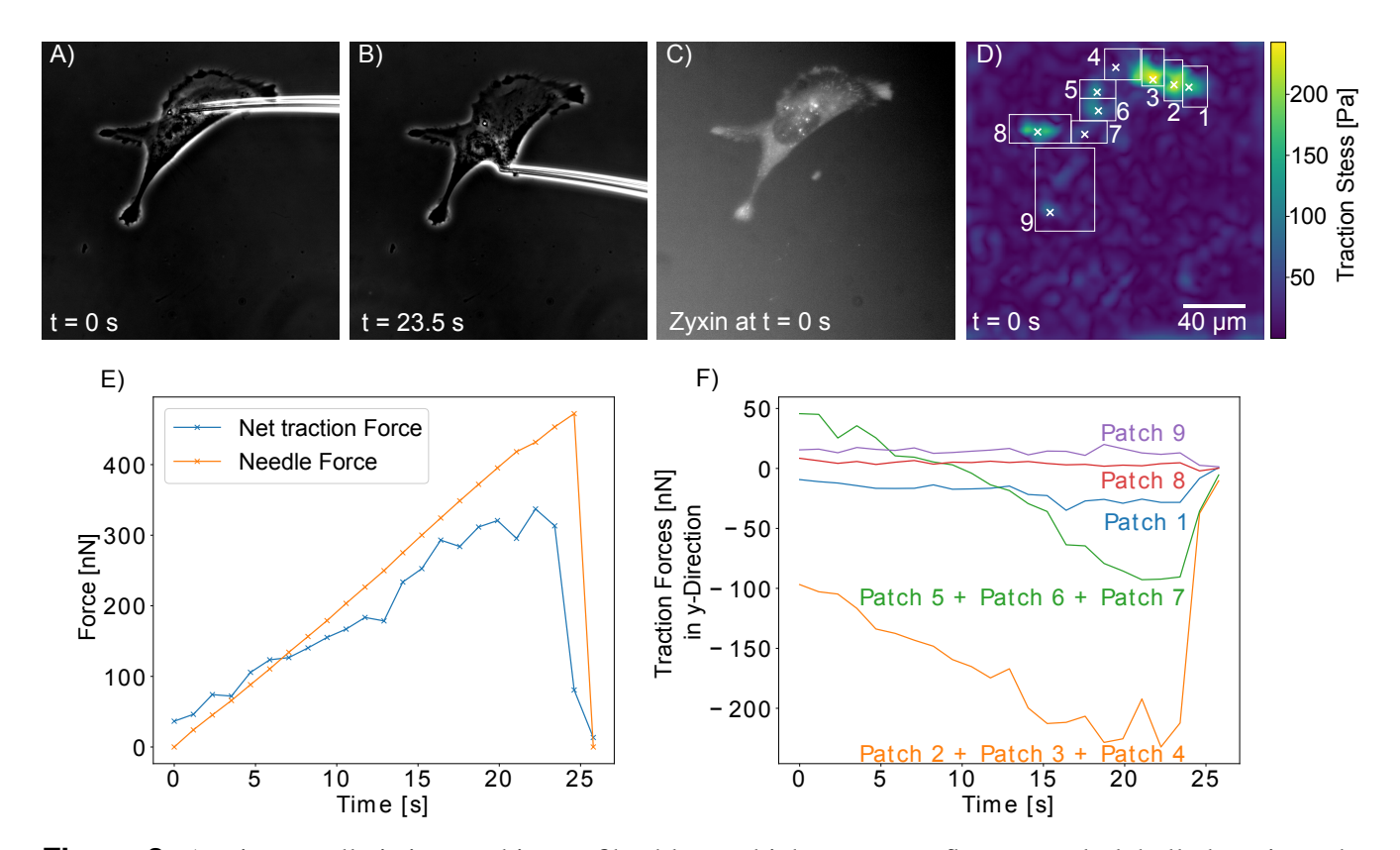


Figure 2. A microneedle is inserted into a fibroblast, which expresses fluorescently labelled zyxin and adheres to a TFM substrate. Subsequently, the needle is moved into the y-direction at a constant speed and exerts shear forces to the cell until it is detached. A) and B) Examplary phase contrast images taken during cell shearing. Both the cell and the needle bending are monitored. The bending of the needle is used to calculate the shear force. C) The cell's zyxin distribution prior to the shearing process is recorded via fluorescence microscopy. D) Traction force map of the cell with adhesion search areas delimited by white rectangles and mean patch locations marked by crosses. Traction forces were reconstructed for t = 0 s using Fourier Transform Traction Cytometry (FTTC). For the reconstruction of traction forces with the shear force monopole present (t > 0), we used the circular patch method.

E) The needle force and the cell's net traction force are plotted as a function of time. F) The traction forces in y-direction are plotted for different adhesion patches (labelled in panel D) to quantify how the cell loads its adhesion sites under the external shearing stimulus.

Due to these limitations, we avoided Fourier space methods^{17,37} and worked directly in real space.

Although continuous force distributions can in principle be reconstructed with the boundary element method (BEM)^{38,39}, here we make additional use of the fact that the cells used in our experiments have well-defined adhesion sites that are increasingly stressed as the cell is sheared by the microneedle.

Motivated by this observation, we use a method where localized forces are distributed inside the cell contour^{40–43}. Rather than using point forces⁴⁰, which also suffer from the divergence problem, we use known contact mechanics solutions for traction forces transmitted on circular areas^{44,45}, for which the

divergence of the Green's function is removed by integration over the contact region. The adhesion forces are estimated using the known deformation-force relation for a constant traction applied over a circular area. Recent studies have suggested that adhesion sites have in fact more elliptic shapes^{36,40,46–48}. This does, however, not have a significant impact on the force reconstruction (see the Supplementary Information for a more thorough discussion). By summing over all adhesion sites and minimizing the deviation between experimental and estimate deformations, one arrives at the theoretical estimate for the traction force field (see the Supplementary Information for more details).

Fig. 2 D shows a traction force map computed with our method. Our algorithm first determines 107 the main sites of traction force transmission from the cell to the PAAm sample. These sites ("adhesion 108 patches") are marked by white crosses and numbers in the figure panel. We calculated the traction force 109 vector of each adhesion patch and then determined the magnitude of the sum of all traction force vectors. This net traction force magnitude was then compared to the needle force. As traction forces without a force 111 monopole are balanced, introducing an externally applied force must result in a change of traction forces 112 to balance the externally applied force. Our results shown in Fig. 2 E demonstrate that the net traction force and the externally applied shear force closely matched during the entire experiment, validating our analysis approach. The fact that the shear force and net traction force do not match perfectly might have 115 several reasons: force can be dissipated²⁴ or cells might resist deformation with cell specific responses. Furthermore, as several calibration steps are needed during force calculations, our results are prone to 117 calibration errors: The needle spring constant was calibrated via shearing a PDMS pillar and the Young's 118 modulus of the PDMS was measured for the computation of the needle's spring constant. Furthermore, 119 the PAAm's Young's modulus needed to be determined in order to reconstruct traction forces from the 120 bead displacement data. Both materials' elastic properties were measured with a state-of-the-art atomic 121 force microscopy procedure³⁴ naturally prone to measurement errors, which means that neither the needle 122 force, nor the traction forces are perfectly accurate. Image analysis inaccuracies in the quantification of 123 the needle bending and bead displacement may further contribute to the slight mismatch between the net 124 traction force and externally applied force. 125

In Fig. 2 F, the y-components of traction force vectors are plotted for the different adhesion patches. For better visualisation, we combined some neighbouring adhesion patches with similar force loading behavior.

126

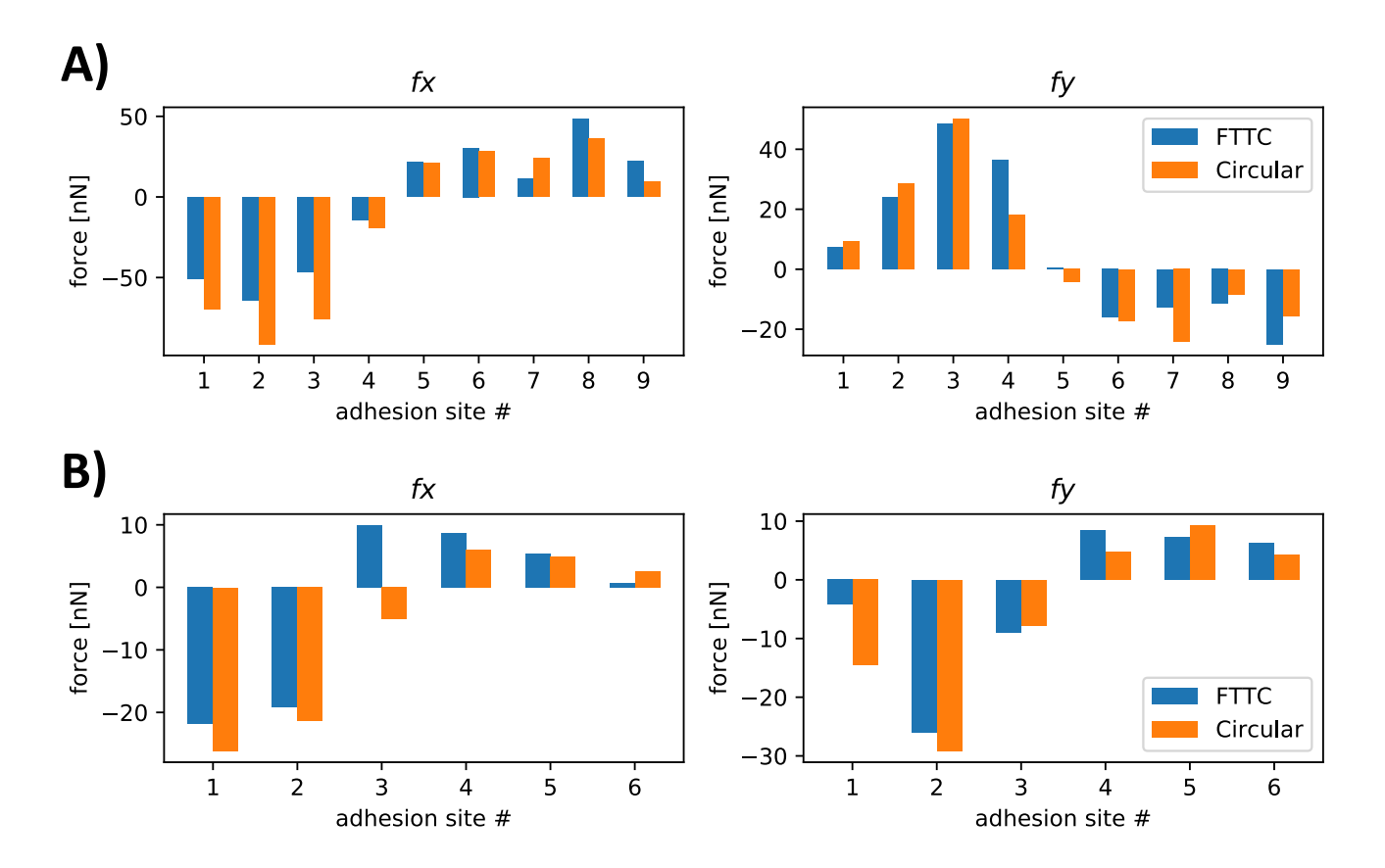


Figure 3. Comparison of the traction forces predicted in the absence of an external force monopole (at t = 0) using the circular patch method (that we employed during this study) and a regularized Fourier Transform Traction Cytometry (FTTC)¹⁴ using generalized cross-validation⁴⁹. A) Profile for the cells introduced in Fig. 2. B) Profile for the cells introduced in Fig. 5. In both cases, the agreement between the two methods is rather good.

The data for each individual adhesion patch is presented in Fig. 5 of the Supplementary Information. As the needle pulled mainly in the y-direction, the x-components of the traction vectors were not influenced by the needle shear force, which is why we concentrate on discussing the y-components (a graph of the x-components of the traction vectors are presented in the supplementary information). One sees that the microneedle pulling mainly loads the adhesion patches 2, 3 and 4, and to a lesser extend also the adhesion patches 5, 6 and 7. This result had to be expected due to the position of these adhesions in the part of the cell that is tensed by the needle. On the other hand, Patches 8 and 9 are not or only slightly loaded, presumably because they are located in the part of the cell subjected to compressive forces during needle shearing. The plot shows that loading is not homogeneous and most likely is related to cytoskeletal elements (e.g. between adhesions and nucleus) not visible here. The asymmetric response of different

adhesion patches can be explained by the fact that the cytoskeleton is made from semiflexible polymers, 138 which respond differently to pulling and pushing. Pulling reduces entropy and increases stretching as well as bending energies, eventually leading to strain stiffening⁵⁰. Pushing, on the other hand, meets little resistance, because cytoskeletal filaments tend to buckle under force and the cytoplasm can flow away, thus it is difficult to locally build up compression energy like in a solid^{51,52}. It is interesting to 142 note that also in the physiological context, cell mechanics is probed mainly in pulling, not in pushing, 143 e.g. in epithelial monolayers, which are under large prestress⁵³. Therefore, pulling is the relevant mode 144 and much more meaningful than pushing. Thus, patches 2 - 7 were loaded presumably because the 145 needle pulling forces were transmitted efficiently to these adhesion patches through the polymers of the 146 cytoskeleton. Correspondingly, patches 8 and 9 were probably not loaded because pushing forces are not 147 transmitted well by cytoskeletal polymers⁵⁴. This is in agreement with earlier studies^{9,10,37}, but our results 148 quantify the traction forces for individual focal adhesion patches under an external mechanical stimulus 149 in an unprecedented way. Our findings also demonstrate the complexity and non-uniform distribution of 150 intracellular force transmission as a function of load and location. 151

The good agreement between the needle force and the net traction force predicted with our circular patch method shown in Fig. 2 E is a first and successful validation of our approach. To further validate it, we reconstructed forces at t = 0 (when there is no force monopole) at single patches with Fourier Transform Traction Cytometry (FTTC) with 0th order Tikhonov regularization¹⁴, where the regularization parameter is determined by generalized cross-validation⁴⁹. Adhesion forces were then calculated by integrating the traction stress in each search window, both for the cell analyzed in Fig. 2 and the cell analyzed in Fig. 5. As shown in Fig. 3, the agreement between the two methods is rather good in both cases.

152

153

154

155

156

157

158

159

Because an unperturbed cell to lowest order forms a force dipole, while the needle presents a force monopole, we next calculated the force moments as a function of time. Because momentum and also angular momentum is not conserved anymore due to the external pulling, one has to be careful how to define these moments (explained in Supplementary Information). Fig. 4 A shows that for the cell shown in Fig. 2, the monopole increases with time, but the major dipole does not decrease as expected. The torque remains low but shows a slight upwards slope. The explanation is provided by Fig. 4 B, which explicitly

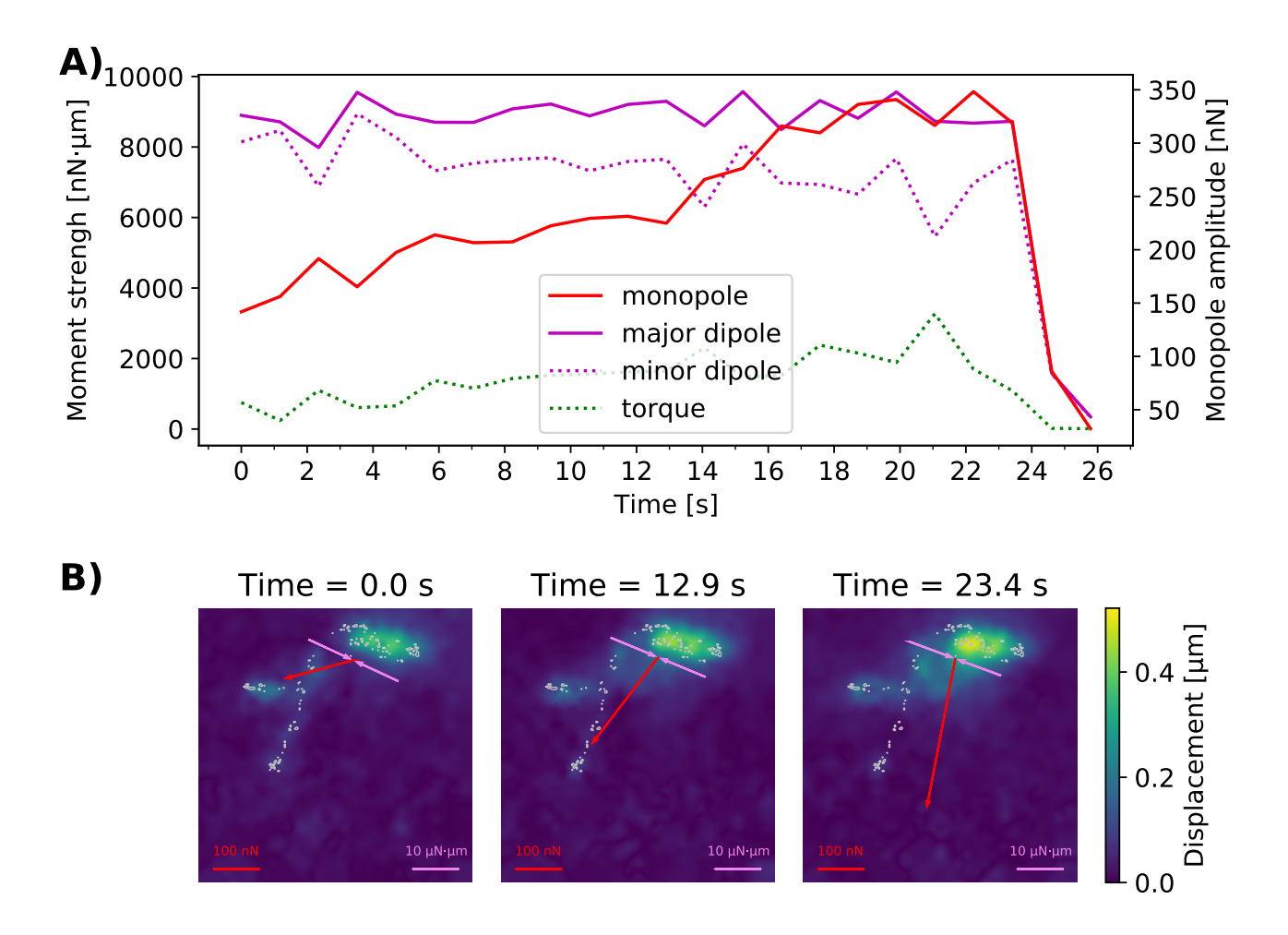


Figure 4. Change of force monopole and dipole moments of the cell presented in Fig. 2 in response to needle shearing. A) presents the magnitudes of the force monopole, as well as the major and minor dipole moments and the torque as functions of time. Our results show that the contractile forces are initially distributed mostly isotropically around the contractile center. However, the force monopole created by the needle shearing increases over time while the minor dipole, which describes the contractility in the direction of the force, deceases slightly. B) shows the force monopole and the major dipole moment in exemplary force maps recorded during the shearing experiment. The force monopole is denoted by red arrows while the dipole moment is represented by purple arrows. The gray encircled regions represent areas where adhesions are predicted from the cell's zyxin distribution.

shows the monopole (in red) and the major dipole (in purple). Because they are oriented perpendicularly to each other, the microneedle pulling does not perturb the cellular dipole for a long time, until complete failure occurs.

We now turn to an example in which monopole and dipole orientations are co-linear. For the cell presented in Fig. 5, only adhesion patches 1, 2 and 3, which - in contrast to patches 4, 5 and 6 - are loaded

169

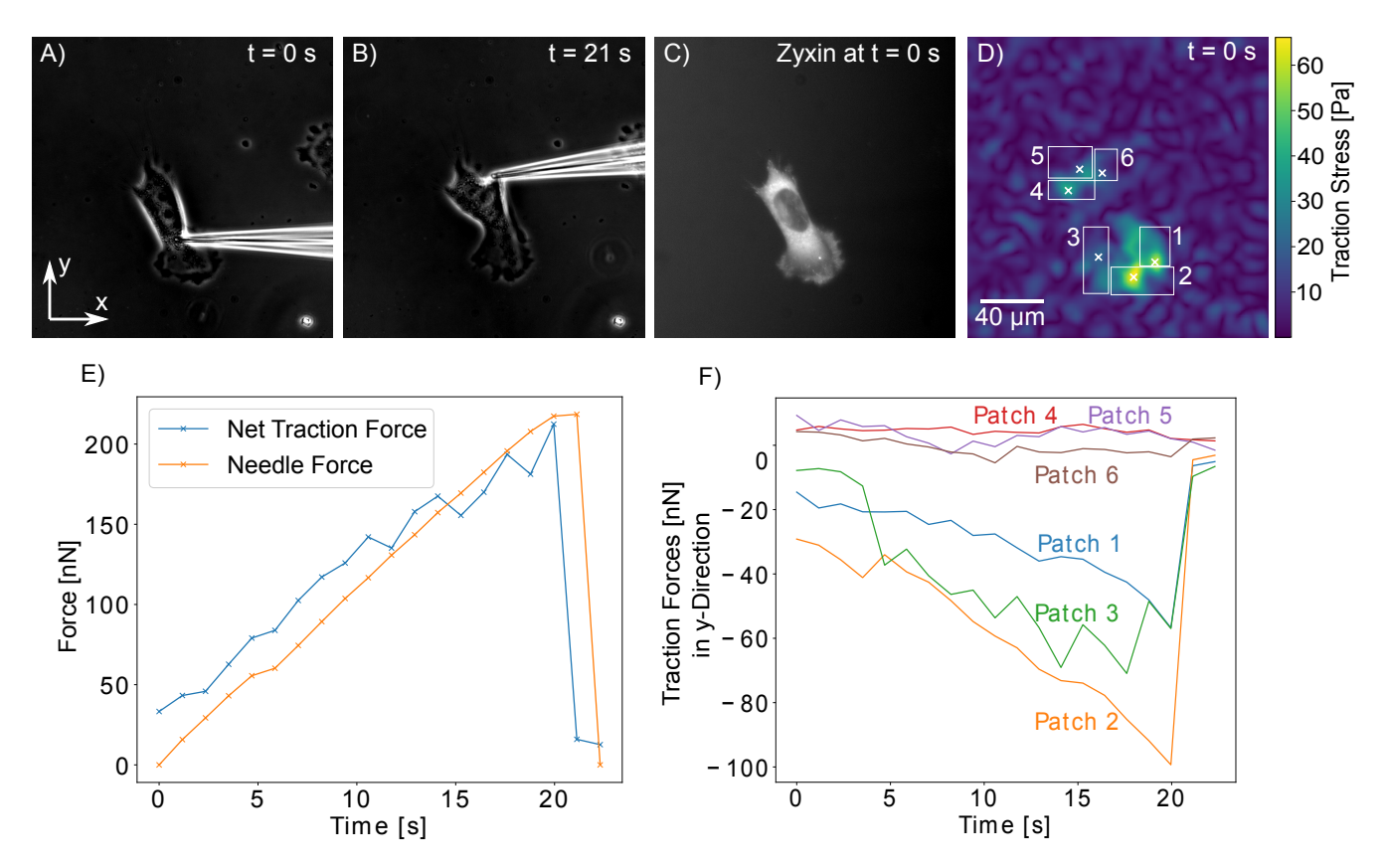


Figure 5. The change of traction forces as a response to microneedle shearing. A) and B) show phase contrast images of a cell adhering to a PAAm substrate and a microneedle exerting shear forces to the cell. The cell's zyxin distribution prior to the shearing process is presented in C) while D) pictures a traction force map with cell's adhesion patch positions marked with white crosses and numbers. The force map is calculated using FTTC at t = 0 s.

In E) The shear force exerted by the needle to the cell is compared to the magnitude of the net traction force vector. The y-components of the traction vectors for the adhesion patches are plotted for each moment of the experiment in F).

in tension, experience an increase in their traction forces. Furthermore, the traction forces exerted through patch 2 change most strongly. This is another indication that force components perpendicular to the shear force vector are not affected by the shearing process as patch 2 lies directly below the site of shear force exertion and thus has much weaker traction forces perpendicular to the shearing direction than patches 1 and 3. Fig. 5 E shows that the total traction forces exerted through the cell have the same magnitude as the needle shear force, which confirms the validity of our approach. In Fig. 6 we plot the force monopole as well as the major and minor dipole moments measured during the experiment presented in Fig. 5 as functions of time. These data demonstrate that the force balance changes from a situation that is governed by the major dipole moment to one dominated by the force monopole that is created by the needle shearing.

While the adhesions in front of the needle are less exposed to the stress, the ones behind are subjected to large tensile cytoskeletal forces. Interestingly, the cellular dipole becomes more and more localized to the tensed region, indicating a strong reorganization or rearrangement also inside the cell. This is supported by the torque that experiences a downward slope indicating that the adhesive center becomes more aligned with the microneedle.

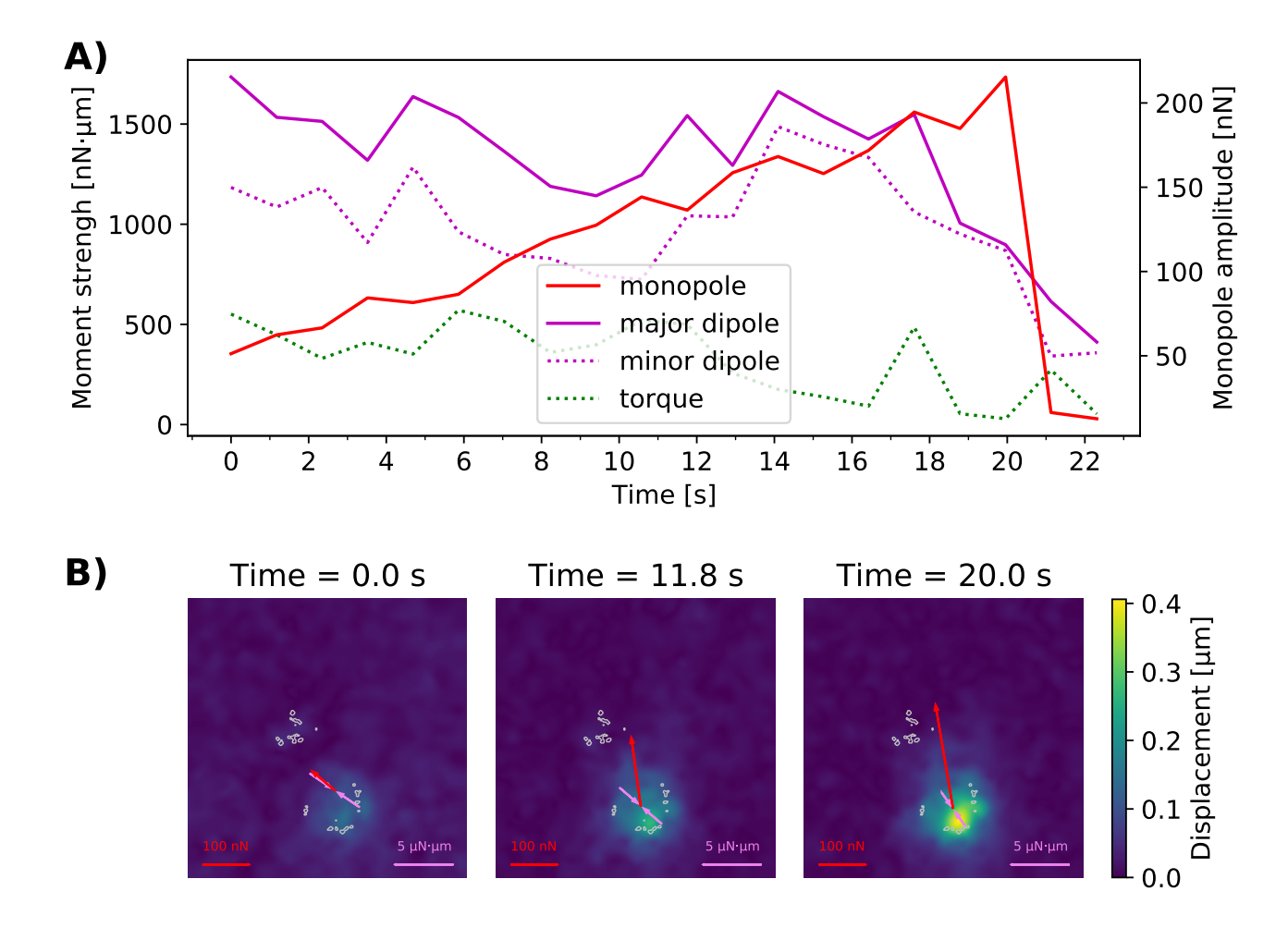


Figure 6. Change of force monopole and dipole moments of the cell presented in Fig. 5 in response to needle shearing. A) presents the magnitudes of the force monopole, as well as the major and minor dipole moments and the torque as functions of time. Our results show that the force balance is initially governed by the major dipole moment. However, the force monopole created by the needle shearing increases over time and governs the force balance at high shearing forces. B) shows the force monopole and the major dipole moment in exemplary force maps recorded during the shearing experiment. The force monopole is denoted by red arrows while the dipole moment is represented by purple arrows. The gray encircled regions represent areas where adhesions are predicted from the cell's zyxin distribution.

The results presented in Fig. 7 show once more that not all adhesion patches are loaded with forces.

Patches 1 as well as 4 and 5 were not loaded under an external shear force. Interestingly, not only patches 186 2 and 3, which were closest to external force application site were loaded, but also adhesion patches 187 10 and 11, even though they were further away from the needle than patches 1, 4 and 5. These data 188 suggest that internal transmission of tension can be long-ranged, for example through stress fibers, as 189 recently demonstrated by optogenetic control of cell contractility⁵⁵. In order to analyse this important 190 aspect in detail, future work has to simultaneously image also the actin cytoskeleton. However, this is very 191 challenging, as we also have to image the zyxin-marked focal adhesions and the fluorescent marker beads 192 in the elastic substrates. 193

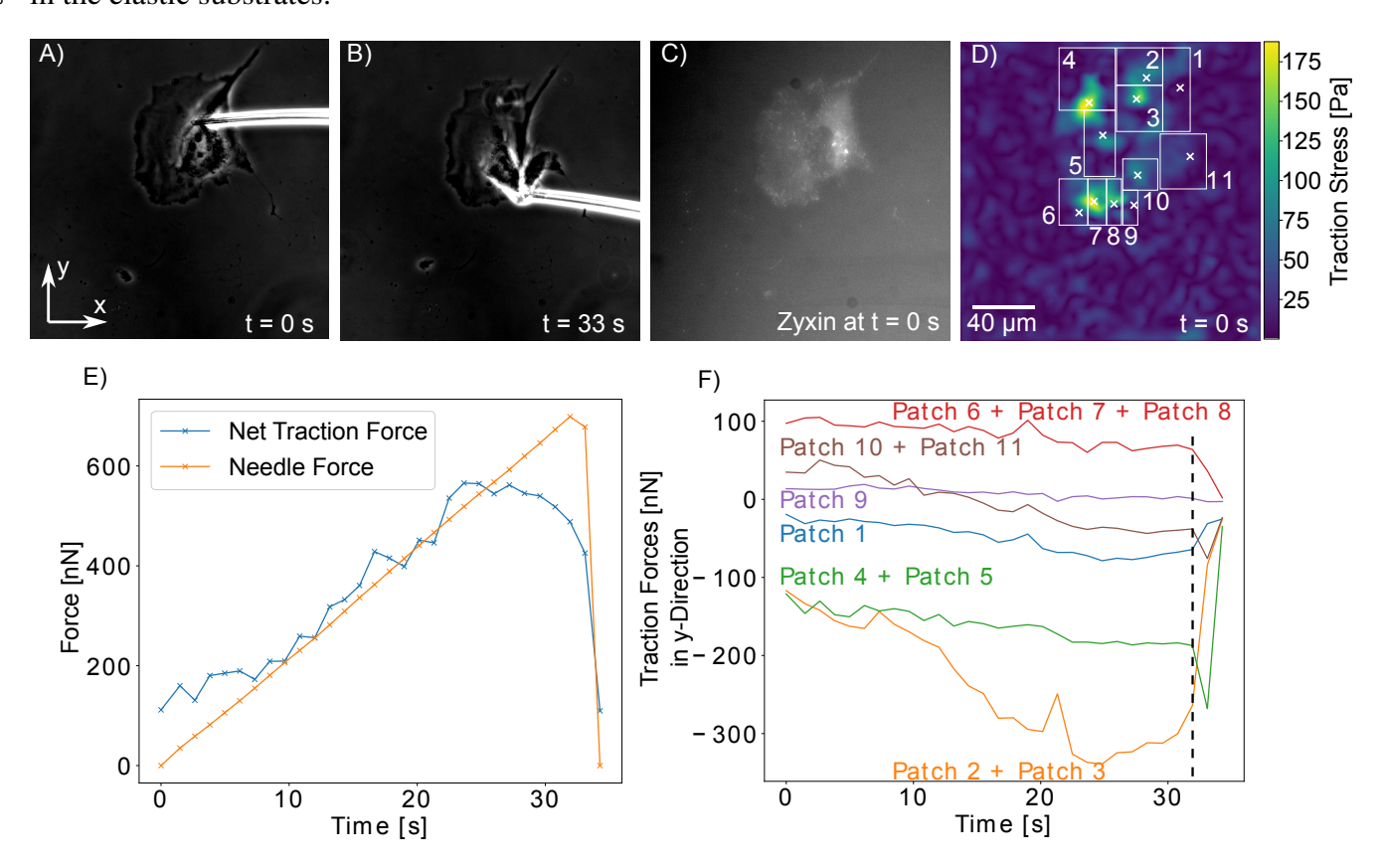


Figure 7. Redistribution of adhesion patch loading after a rupture event. A) and B) show phase contrast images of a microneedle shearing a fibroblast on a PAAm substrate. The cell's zyxin distribution is visualized in C). A map of the traction forces at t = 0 s exerted at the cell's adhesion patches is presented in D). The white crosses mark the cell's adhesion sites. The force map is calculated using FTTC at t = 0 s. The sum of traction forces has roughly the same magnitude as the external shear force, as can be seen in E). The y-components of the traction vectors for the adhesion patches are plotted in F). The dashed line marks the rupture of adhesion patches 1, 2 and 3 at t = 32 s

It is a well-established fact that focal adhesions rupture successively under external forces²⁴, nonetheless our results presented in Fig. 7 quantify for the first time the redistribution of traction forces throughout

194

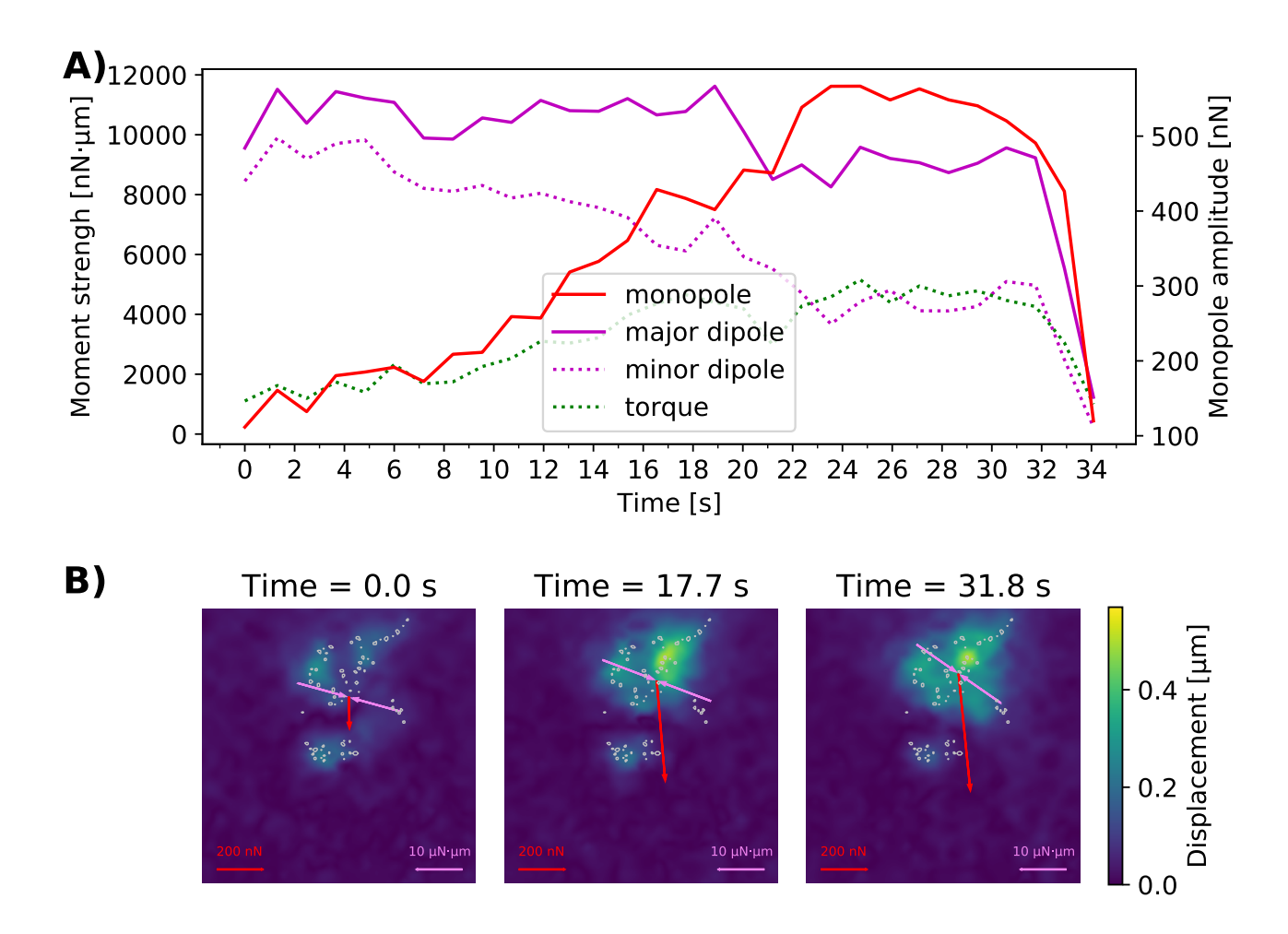


Figure 8. Change of force monopole and dipole moments of the cell presented in Fig. 7 in response to needle shearing. A) presents the magnitudes of the force monopole, as well as the major and minor dipole moments and the torque as functions of time. Our results show that the force balance is initially governed by the major dipole moment. However, the force monopole created by the needle shearing increases over time and governs the force balance at high shearing forces. B) shows the force monopole and the major dipole moment in exemplary force maps recorded during the shearing experiment. The force monopole is denoted by red arrows while the dipole moment is represented by purple arrows. The gray encircled regions represent areas where adhesions are predicted from the cell's zyxin distribution.

the cell after the rupture of adhesion sites. When adhesion patches 1, 2 and 3 ruptured after 32 s (marked by the dashed line) - even though adhesion patch 1 had barely been loaded with force before that - the traction forces exerted through all other patches except patch 9 increased substantially. Interestingly, patches 10 and 11, which had been the only patches that were loaded strongly prior to the rupture event, were only loaded with a small amount of force upon the rupture event, while patches 4 and 5, which had been only marginally loaded, changed their traction forces much more strongly following the rupture

event. In the future, one might use adhesive micropatterns to control the exact location of the adhesion patches and therefore the way individual adhesion sites are loaded by the shearing force.

In Fig. 8 we present the force monopole as well as the major and minor dipole moments measured during the experiment presented in Fig. 7 as functions of time. The behavior is similar to the one presented in Fig. 6.

Another striking aspect is the fact that the traction forces exerted through patches 2 and 3 started to 207 slowly decrease several seconds prior to the rupturing event. We observed a similar behavior for adhesion 208 patch 3 of the cell presented in Fig. 5. This suggests that the rupture of focal adhesions is not necessarily 209 an instantaneous event, but that there exist rupture processes of extended duration, which we recorded 210 using our novel analysis approach. Strikingly, the load on some focal adhesions decreased prior to rupture 211 while in others, the traction forces increased until they ruptured. Similar differences in adhesion site 212 behavior have been described before as slip bonds and catch bonds⁵⁶, but in our experimental setting, 213 which analyzes the behaviour of intact cells, the mechanical properties of the cell and force transmission through the cytoskeleton likely play an important role, too. Our new technique hence enables us to reveal possible physical factors that influence dynamic changes in force loading of adhesion sites.

Conclusion

204

205

206

We have introduced a novel method for determining traction forces in cells under external shear forces. The 218 applicability of our method has been proven by shearing fibroblasts off their underlying PAAm substrates 219 while monitoring the change in cellular traction forces at specific adhesion sites. We have shown that 220 cells on soft substrates distribute an external shear force non-uniformly among their adhesion sites, as a 221 function of location and load (tensile vs. compressive). Notably, we found that force transmission can be 222 long ranged and mainly applies to adhesions that are under tensile load. This result may be due to the 223 polymeric nature of the cytoskeletal network, which is better suited for the transmission of tensile forces. 224 As our technique monitors the change in traction forces simultaneously to the shearing stimulation, it introduces a new quality to the recordings of rupture events to complement conventional techniques such 226 as the single-cell force spectroscopy. Indeed, our method can be easily adapted to other force exertion 227 methods and hence is very versatile and complementary to existing procedures. In the future, it could

be combined with imaging of the cytoskeleton to achieve a more complete understanding of how force is transmitted through the cell. Moreover adhesive micropatterns might be used to better control the positioning of the adhesion patches; with these two elements in place, we expect that our method can be used to achieve a comprehensive understanding of how force is transmitted through adherent cells.

Materials and Methods

234 Cell Culture

Mouse embryonic fibroblasts expressing mNeonGrenn labeled zyxin were cultured at 37°C in 21% O₂, 5% CO₂ at a humidity of 95%. Dulbecco's Modified Eagle Medium (DMEM; Biochrom) containing 10% fetal bovine serum (FBS; Biochrom) and 1% penicillin/streptomycin (pen strep; $10.000 \,\mu g/ml$; Biochrom) 237 served as cell culture medium. Cells were seeded on a PAAm sample by removing the cell culture medium 238 and rinsing the cells at a confluency of about 80 % with PBS. The cells were incubated in trypsin/EDTA 239 (0.5%/0.2% in 10xPBS; Biochrom) at 37°C for 1 minute. Cell culture medium was added to stop the 240 trypsination process and the cells were seperated from the liquids via 5 min of centrifugation at 2412 rpm. 241 The supernatant was replaced by fresh cell culture medium. The cells were redispersed and 100 µl of cell 242 suspension added to a PAAm sample with another 900 µl of DMEM. The cells were allowed to spread on 243 the PAAm sample overnight at 37°C prior to shearing experiments.

5 Polyacrylamide Preparation

A \(\noting 50 \) mm FluoroDish Cell Culture Dish (World Precision Instruments) was pretreated to promote PAAm 246 attachement. They were cleaned three times with ethanol and double-distilled water before being incubated 247 in sodium hydroxide (NaOH, 2.5 M) for 10 min. Subsequently, the slides were cleaned in an ultrasonic 248 bath in double-distilled water for 10 min, rinsed with ethanol and incubated for 15 min in a mixture of 249 97 % ethanol (absolute), 2 % 3-(Trimethoxysilyl)propyl methacrylate (Sigma-Aldrich) and 1 % acetic acid 250 (Sigma-Aldrich). Subsequently, they were rinsed with ethanol and dried in air. A marker bead solution 251 was prepared by adding 100 µl fluorescent beads (1% solids, nominal \(\notin \) 50nm, Flash Red, Bangslabs, 252 Cat. No. FSFR001) in 900 µl double-distilled water. The solution was cleaned twice by centrifuging and 253 replacing of the supernatant with double-distilled water.

PAAm was produced by degassing a solution of 150 acrylamide µl (40%; Biorad), 90 µl bis-acrylamide 255 (bis; 2%; Biorad), 10 µl 4-(2-hydroxyethyl)-1-piperazineethanesulfonic acid buffer (HEPES; 0.5 mM; 256 pH = 7; Biochrom), 255 μl aqueous Acrylic acid N-hydroxysuccinimide ester solution (2 wt%, Sigma-257 Aldrich, CAS No 38862-24-7), 3 µl NaOH (2.5 M), and 10 µl marker bead solution in vaccum for 20 min. Subsequently, 2.5 µl ammoniumperoxodisulfate (10 wt% in aqueous solution; Sigma-Aldrich; CAS No 259 7727-54-0) and 0.375 µl N,N,N',N'-Tetramethylethylenediamine (TEMED, Sigma-Aldrich, CAS No 260 110-18-9) were added to 260 μl of the acrylamide solution. After thoroughly mixing the solution, 10 μl 261 were deposited into a pretreated FluoroDish and covered with a round \(\notin \) 18 \(\mu \) coverslip. The sample 262 was left to polymerize in darkness for 30 min before the coverslip was removed. The sample was soaked 263 in double distilled water for 3 days. The water was removed and the sample was incubated in 100 µl 264 fibronectin (aqueous 100 μg/ml solution) overnight at 6°C. The sample was shaken in 70% ethanol for 265 10 min and rinsed three times with sterile double-distilled water. Cells were added and allowed to spread 266 overnight prior to shearing experiments. Young's modulus of exemplary PAAm samples were measured to 267 be 16.5 ± 0.5 kPa employing our priorly published procedure³⁴. Details are published in the supplementary 268 information. 269

270 Microneedle Preparation

Microneedles were pulled from hollow borosilicate glass tubes (outer diameter 1 mm, inner diameter 0.5 mm, length 100 mm, item #: B100-50-10, Sutter Instruments Co.) using a Flaming/Brown micropipette puller (Model P-97, Sutter Instruments Co.). The employed parameters were Pressure = 500, Heat = 490, Velocity = 70, Pull = 70, Time = 100. For descriptions of these parameters please refer to⁵⁷. A MF-900 Microforge (NARISHIGE Group) was used to bend the needle so that the tip and base form an angle of about 45°. Each needle was installed into a micromanipulator so that its tip is parallel to the sample surface.

Microneedle Calibration

Each time a needle was installed to the micromanipulator, its spring constant was calibrated prior to cell shearing experiments by shearing the needle against a PDMS pillar. Prior to calibration, a PDMS sample with a network of 6 μm long pillars with a radius of 2 μm was soaked in water and degassed in vaccum for

10 minutes to remove air bubbles. The microneedle was positioned next to a PDMS pillar. The optimum 282 needle height was determined by lowering the microneedle in 1 µm steps and trying to shear the pillar after 283 each step to see if the needle slips before the pillar bends. Subsequently, the needle was moved against 284 the pillar at 2 µm/s while phase contrast images were recorded at a frame rate of 0.85 fps. At least one image of the unbent needle was aquired before the shearing process was initiated. This image served as a 286 reference for calculation of needle bending. To erradicate errors from needle assymetry, the direction of 287 needle movement was chosen to be the same during cell shearing experiments and during the calibration 288 process. To calculate the spring constant, the positions of the needle tip and the PDMS pillar were tracked 289 manually in phase contrast images with imageJ. The respective positions in the reference frame were 290 subtracted to compute the distances the tip had moved and the PDMS pillar had bent. For each frame, the 291 time stamps of the phase contrast images were employed to calculate how much time has passed since 292 the needle movement had started. This duration was multiplied with the speed of needle movement to 293 compute the distance the needle had moved. The microneedle bending was calculated as the difference 294 between micromanipulator distance and needle tip distance. The force necessary to bend a PDMS pillar 295 was calculated as published by Schoen et al. 35. Young's modulus of the PDMS sample had been measured 296 to be 801.5 ± 32.9 kPa employing our previously published procedure³⁴. The pillar force was plotted 297 versus the needle bending and a linear fit is employed to calculate the slope of the resulting curve that 298 corresponds to needles spring constant. We present an exemplary calibration experiment as well as details 299 on the determination of the PDMS sample's Young's modulus in the supplementary information.

301 Shearing Process and Shear Force Calculation

A fluorescence image of the zyxin distribution of a well-spread fibroblast was recorded. The calibrated microneedle was inserted into this cell directly above or below the nucleus and a phase contrast image of cell and needle was recorded. Subsequently, the needle was moved horizontally at 5 μm/s against the nucleus. During the shearing process, phase contrast images of cell and needle as well as fluorescent images of the marker beads embedded in the underlying PAAm substrate were recorded alternately at a frame rate of 0.85 fps. After cell detachment, an additional pair of fluorescent microscopy and phase contrast images was recorded. This last fluorescent image pair recorded the bead position of the

PAAm sample without any influence of traction forces and served as reference image for traction force calculations.

Images were recorded using an inverted microscope (Z1 Observer, Zeiss) equipped with a CMOS
Camera (Hamamatsu ORCA Flash 4.0) and a 40x objective with phase contrast (Zeiss EC Plan-Neofluar
40x/0.75 Ph2 M27). Both, the phase contrast images and the fluorescence images were recorded using
the RFP filtercube (necessary to image the fluorescent marker beads) to minimize the time between
the measurement of shear force and traction forces. The microneedle was handled using a Eppendorf
InjectMan NI2 micromanipulator. For each frame, the bending of the needle was calculated as described
in the calibration section above. The shear force was computed by multiplying the needle bending with
the needle's spring constant calibrated prior to each experiment.

Calculation of Traction Forces

Traction forces were calculated using a home-written algorithm that employs the established deformation-320 force relation for a constant traction applied over a circular area. A single adhesion was assumend per 321 area. The location of each adhesion center within each area was determined for each frame using the local maxima approach. The adhesion radius was found by inspecting the surrounding peaks. A common radius 323 was determined for each adhesion, which was then used for all frames. A detailed description can be found 324 in the supplementary information. The substrate deformation field was obtained from fluorescent bead 325 images using PIV^{58,59}. A windows size of 64 pixels and a 50% window overlap was used. Spurious vectors 326 were removed using a minimal signal-to-noise ratio in the correlation function of 1.5 and a threshold of 327 2.0 for the normalized median test. The reference image was taken after cell detachment. 328

References

- Jaalouk, D. E. & Lammerding, J. Mechanotransduction gone awry. *Nat. Rev. Mol. Cell Biol.* 10, 63–73, DOI: 10.1038/nrm2597 (2009).
- Petridou, N. I., Spiró, Z. & Heisenberg, C. P. Multiscale force sensing in development. *Nat. Cell Biol.* 19, 581–588, DOI: 10.1038/ncb3524 (2017).

- 3. Roca-Cusachs, P., Conte, V. & Trepat, X. Quantifying forces in cell biology. *Nat. Cell Biol.* **19**, 742 751, DOI: 10.1038/ncb3564 (2017).
- 4. Paluch, E. K. *et al.* Mechanotransduction: use the force(s). *BMC Biol.* 13, 47, DOI: 10.1186/s12915-015-0150-4 (2015).
- 5. Lv, H. *et al.* Mechanism of regulation of stem cell differentiation by matrix stiffness. *Stem Cell Res.*Ther. 6, 1–11, DOI: 10.1186/s13287-015-0083-4 (2015).
- 6. Engler, A. J., Sen, S., Sweeney, H. L. & Discher, D. E. Matrix Elasticity Directs Stem Cell Lineage
 Specification. *Cell* 126, 677–689, DOI: 10.1016/j.cell.2006.06.044 (2006).
- 7. Cui, Y. *et al.* Cyclic stretching of soft substrates induces spreading and growth. *Nat. Commun.* **6**, 1–8, DOI: 10.1038/ncomms7333 (2015).
- 8. Brugués, A. *et al.* Forces driving epithelial wound healing. *Nat. Phys.* 10, 683–690, DOI: 10.1038/
 NPHYS3040 (2014).
- 9. Riveline, D. *et al.* Focal Contacts as Mechanosensors: Externally Applied Local Mechanical Force
 Induces Growth of Focal Contacts by an Mdia1-Dependent and Rock-Independent Mechanism. *J. Cell Biol.* 153, 1175–1186, DOI: 10.1083/jcb.153.6.1175 (2001).
- 10. Paul, R., Heil, P., Spatz, J. P. & Schwarz, U. S. Propagation of mechanical stress through the actin cytoskeleton toward focal adhesions: Model and experiment. *Biophys. J.* 94, 1470–1482, DOI: 10.1529/biophysj.107.108688 (2008).
- 11. Davies, P. F. Flow-mediated endothelial mechanotransduction. *Physiol. reviews* 75, 519–560 (1995).
- 12. Perrault, C. M. *et al.* Traction Forces of Endothelial Cells under Slow Shear Flow. *Biophys. J.* 109,
 1533–1536, DOI: 10.1016/j.bpj.2015.08.036 (2015).
- 13. Lo, C.-M., Wang, H.-B., Dembo, M. & Wang, Y.-L. Cell movement is guided by the rigidity of the substrate. *Biophys. J.* 79, 144–152, DOI: 10.1016/S0006-3495(00)76279-5 (2000).
- 14. Schwarz, U. S. & Soiné, J. R. Traction force microscopy on soft elastic substrates: A guide to recent computational advances. *Biochimica et Biophys. Acta Mol. Cell Res.* 1853, 3095–3104, DOI: 10.1016/j.bbamcr.2015.05.028 (2015). 1506.02394.

- 15. Style, R. W. *et al.* Traction force microscopy in physics and biology. *Soft Matter* 10, 4047–4055,
 DOI: 10.1039/c4sm00264d (2014).
- 16. Kronenberg, N. M. *et al.* Long-term imaging of cellular forces with high precision by elastic resonator interference stress microscopy. *Nat. Cell Biol.* **19**, 864–872, DOI: 10.1038/ncb3561 (2017).
- 17. Sabass, B., Gardel, M. L., Waterman, C. M. & Schwarz, U. S. High resolution traction force
 microscopy based on experimental and computational advances. *Biophys. J.* 94, 207–220, DOI:
 10.1529/biophysj.107.113670 (2008).
- 18. Balaban, N. Q. *et al.* Force and focal adhesion assembly: a close relationship studied using elastic micropatterned substrates. *Nat. Cell Biol.* **3**, 466–472 (2001).
- 19. Vishwakarma, M. *et al.* Mechanical interactions among followers determine the emergence of leaders in migrating epithelial cell collectives. *Nat. Commun.* 9, DOI: 10.1038/s41467-018-05927-6 (2018).
- 20. Hino, N. *et al.* ERK-Mediated Mechanochemical Waves Direct Collective Cell Polarization. *Dev. Cell* 53, 646–660.e8, DOI: 10.1016/j.devcel.2020.05.011 (2020). Publisher: Elsevier.
- 21. Ng, M. R., Besser, A., Brugge, J. S. & Danuser, G. Mapping the dynamics of force transduction at cell–cell junctions of epithelial clusters. *eLife* 3, e03282, DOI: 10.7554/eLife.03282 (2014).
- 22. Das, T. *et al.* A molecular mechanotransduction pathway regulates collective migration of epithelial cells. *Nat. Cell Biol.* 17, 276–287, DOI: 10.1038/ncb3115 (2015).
- 23. Kadem, L. F. *et al.* Rapid Reversible Photoswitching of Integrin-Mediated Adhesion at the Single-Cell Level. *Adv. Mater.* 28, 1799–1802, DOI: 10.1002/adma.201504394 (2016).
- 24. Selhuber-Unkel, C. *et al.* Cell adhesion strength is controlled by intermolecular spacing of adhesion receptors. *Biophys. J.* 98, 543–551, DOI: 10.1016/j.bpj.2009.11.001 (2010).
- 25. Huth, S., Reverey, J. F., Leippe, M. & Selhuber-Unkel, C. Adhesion forces and mechanics in mannose-mediated acanthamoeba interactions. *PLOS ONE* **12**, e0176207 (2017).
- 26. Brunner, C. A. *et al.* Cell migration through small gaps. *Eur. Biophys. J.* 35, 713–719, DOI: 10.1007/s00249-006-0079-1 (2006).

- ³⁸⁵ **27.** Hanke, J., Ranke, C., Perego, E. & Köster, S. Human blood platelets contract in perpendicular direction to shear flow. *Soft matter* **15**, 2009–2019 (2019).
- 28. Rief, M., Oesterhelt, F., Heymann, B. & Gaub, H. E. Single Molecule Force Spectroscopy on Polysaccharides by Atomic Force Microscopy. *Science* 275, 1295 LP 1297, DOI: 10.1126/science. 275.5304.1295 (1997).
- 29. Neuman, K. C. & Nagy, A. Single-molecule force spectroscopy: optical tweezers, magnetic tweezers and atomic force microscopy. *Nat. Methods* **5**, 491–505, DOI: 10.1038/nmeth.1218 (2008).
- 392 **30.** Jiang, G., Giannone, G., Critchley, D. R., Fukumoto, E. & Sheetz, M. P. Two-piconewton slip bond between fibronectin and the cytoskeleton depends on talin. *Nature* **424**, 334–337, DOI: 10.1038/ nature01805 (2003).
- 31. Fedorchak, G. & Lammerding, J. Cell Microharpooning to Study Nucleo-Cytoskeletal Coupling. In
 Shackleton, S., Collas, P. & Schirmer, E. C. (eds.) *The Nuclear Envelope: Methods and Protocols*,
 chap. 16, 241–254 (Springer Science+Business Media New York, New York, 2016).
- 32. Chan, C. *et al.* Myosin II Activity Softens Cells in Suspension. *Biophys. J.* **108**, 1856–1869, DOI: 10.1016/j.bpj.2015.03.009 (2015).
- Micoulet, A., Spatz, J. P. & Ott, A. Mechanical Response Analysis and Power Generation by
 Single-Cell Stretching. *ChemPhysChem* 6, 663–670, DOI: https://doi.org/10.1002/cphc.200400417
 (2005).
- 34. Huth, S., Sindt, S. & Selhuber-Unkel, C. Automated analysis of soft hydrogel microindentation:
 Impact of various indentation parameters on the measurement of Young's modulus. *PLoS ONE* 14,
 e0220281, DOI: 10.1371/journal.pone.0220281 (2019).
- 35. Schoen, I., Hu, W., Klotzsch, E. & Vogel, V. Probing cellular traction forces by micropillar arrays:
 Contribution of substrate warping to pillar deflection. *Nano Lett.* 10, 1823–1830, DOI: 10.1021/
 nl100533c (2010).
- 36. Soiné, J. R. D. *et al.* Model-based traction force microscopy reveals differential tension in cellular actin bundles. *PLOS Comput. Biol.* 11, e1004076, DOI: 10.1371/journal.pcbi.1004076 (2015).

- strain energy that cells exert on their surroundings. *Am. J. Physiol. Physiol.* **282**, C595–C605, DOI: 10.1152/ajpcell.00270.2001 (2002).
- 38. Dembo, M. & Wang, Y.-L. Stresses at the cell-to-substrate interface during locomotion of fibroblasts.

 Biophys. J. 76, 2307–2316, DOI: 10.1016/s0006-3495(99)77386-8 (1999).
- Han, S. J., Oak, Y., Groisman, A. & Danuser, G. Traction microscopy to identify force modulation in subresolution adhesions. *Nat. Methods* **12**, 653–656, DOI: 10.1038/nmeth.3430 (2015).
- 418 **40.** Schwarz, U. *et al.* Calculation of forces at focal adhesions from elastic substrate data: The effect
 419 of localized force and the need for regularization. *Biophys. J.* **83**, 1380–1394, DOI: 10.1016/
 420 s0006-3495(02)73909-x (2002).
- 41. Delanoë-Ayari, H., Rieu, J. P. & Sano, M. 4d traction force microscopy reveals asymmetric cortical forces in MigratingDictyosteliumCells. *Phys. Rev. Lett.* **105**, DOI: 10.1103/physrevlett.105.248103 (2010).
- 424 **42.** Schoen, I., Pruitt, B. L. & Vogel, V. The yin-yang of rigidity sensing: How forces and mechanical properties regulate the cellular response to materials. *Annu. Rev. Mater. Res.* **43**, 589–618, DOI: 10.1146/annurev-matsci-062910-100407 (2013).
- 43. Aramesh, M. *et al.* Functionalized bead assay to measure three-dimensional traction forces during t-cell activation. *Nano Lett.* **21**, 507–514, DOI: 10.1021/acs.nanolett.0c03964 (2020).
- 44. Johnson, K. L. Contact Mechanics (Cambridge University Press, 1985).
- 430 **45.** Huang, Y., Gompper, G. & Sabass, B. A bayesian traction force microscopy method with automated denoising in a user-friendly software package. *Comput. Phys. Commun.* **256**, 107313 (2020).
- 432 **46.** Kim, D.-H. & Wirtz, D. Focal adhesion size uniquely predicts cell migration. *The FASEB J.* **27**, 1351–1361, DOI: https://doi.org/10.1096/fj.12-220160 (2013). https://faseb.onlinelibrary.wiley.com/doi/pdf/10.1096/fj.12-220160.
- 47. Zamir, E. *et al.* Molecular diversity of cell-matrix adhesions. *J. cell science* 112 (Pt 11), 1655–69,
 DOI: 10.1242/jcs.112.11.1655 (1999).

- 48. Prager-Khoutorsky, M. *et al.* Fibroblast polarization is a matrix-rigidity-dependent process controlled by focal adhesion mechanosensing. *Nat. Cell Biol.* **13**, 1457–1465, DOI: 10.1038/ncb2370 (2011).
- 49. Huang, Y. *et al.* Traction force microscopy with optimized regularization and automated Bayesian parameter selection for comparing cells. *Sci. Reports* **9**, 539, DOI: 10.1038/s41598-018-36896-x (2019).
- 50. Storm, C., Pastore, J. J., MacKintosh, F. C., Lubensky, T. C. & Janmey, P. A. Nonlinear elasticity in biological gels. *Nature* 435, 191–194, DOI: 10.1038/nature03521 (2005).
- 51. Brangwynne, C. P. *et al.* Microtubules can bear enhanced compressive loads in living cells because of lateral reinforcement. *The J. Cell Biol.* 173, 733 741, DOI: 10.1083/jcb.200601060 (2006).
- 52. Bischofs, I. B., Klein, F., Lehnert, D., Bastmeyer, M. & Schwarz, U. S. Filamentous network
 mechanics and active contractility determine cell and tissue shape. *Biophys. journal* 95 7, 3488–96,
 DOI: 10.1529/biophysj.108.134296 (2008).
- 53. Harris, A. R. *et al.* Characterizing the mechanics of cultured cell monolayers. *Proc. Natl. Acad. Sci.* 109, 16449 16454, DOI: 10.1073/pnas.1213301109 (2012).
- 54. Gardel, M. L., Kasza, K. E., Brangwynne, C. P., Liu, J. & Weitz, D. A. Chapter 19: Mechanical
 response of cytoskeletal networks. *Methods cell biology* 89, 487–519, DOI: 10.1016/S0091-679X(08)
 00619-5 (2008).
- 55. Oakes, P. W. *et al.* Optogenetic control of RhoA reveals zyxin-mediated elasticity of stress fibres. *Nat. Commun.* 8, 15817, DOI: 10.1038/ncomms15817 (2017).
- 56. Pereverzev, Y. V., Prezhdo, O. V., Forero, M., Sokurenko, E. V. & Thomas, W. E. The Two-Pathway
 Model for the Catch-Slip Transition in Biological Adhesion. *Biophys. J.* 89, 1446–1454, DOI:
 10.1529/BIOPHYSJ.105.062158 (2005).
- 57. Oesterle, A. Micropipette CookBook Sutter Instrument Co. (2018).
- 58. Westerweel, J. Fundamentals of digital particle image velocimetry. *Meas. Sci. Technol.* 8, 1379–1392, DOI: 10.1088/0957-0233/8/12/002 (1997).

Taylor, Z. J., Gurka, R., Kopp, G. A. & Liberzon, A. Long-duration time-resolved piv to study unsteady aerodynamics. *IEEE Transactions on Instrumentation Meas.* **59**, 3262–3269, DOI: 10.1109/tim.2010.2047149 (2010).

465 Acknowledgements

468

471

476

- C. S. and S. H. acknowledge support through the ERC CellInspired (Starting grant no. 336104, Proof of Concept Grant no. 768740).
- C. S., U. S. S. and J.B. acknowledge funding by the DFG under Germany's Excellence Strategy 2082/1-390761711 (Cluster of excellence 3D Matter Made to Order).
- J. B. thanks the Carl Zeiss Foundation for financial support.
- C. S. and U. S. S. acknowledge funding through the Max Planck School Matter to Life supported by the
 German Federal Ministry of Education and Research (BMBF).
- J. L. and C. S. acknowledge funding by the Volkswagen Foundation "Life?" program (award A130142).
- J.L. acknowledges funding from the National Institutes of Health (awards U54 210184, R01 HL082792,
 R01 GM137605).

Quantifying Force Transmission through Fibroblasts: Changes of Traction Forces under External Shearing Supplementary Information

Steven Huth, Johannes Blumberg, Dimitri Probst, Jan Lammerding, Ulrich S. Schwarz and Christine Selhuber-Unkel

Reconstruction of traction forces

In our analysis, we assume that focal adhesions, where force is transmitted to the substrate, have a circular shape. For the far field, it is not essential whether the traction forces within an adhesion are distributed evenly or vary over this area, for example decaying towards the rim. In any case, the far field would result in the Green's function of the elastic halfspace, which represents a point force in the middle of the adhesion [1]. For the near field, the solutions looks slightly different. Therefore the main difference between different assumptions would be the reconstruction of the forces in the middle of the focal adhesions. To compare the effect of different assumptions, we initially consider two types of circular adhesive patterns: the constant traction force patterns and radial decreasing Hertz-like traction force pattern.

The analytical solution for the surface deformation created by a tangential traction force $\mathbf{F} = (F_x, F_y)^T$ distributed equally over a circular area with radius a at the surface of a sufficiently thick, substrate in the linear, isotropic elastic regime has recently been calculated in the context of traction force microscopy [2]. Employing polar coordinates $\mathbf{r} = r(\cos \theta, \sin \theta)$ centered around the middle of the circular adhesion, the surface traction profile is given by:

$$\boldsymbol{\tau}(r,\theta) = \begin{cases} \frac{\mathbf{F}}{\pi a^2} & r < a \\ 0 & r \ge a \end{cases} \tag{1}$$

The corresponding deformation field is given by

$$u_x(r,\theta) = \frac{1+\nu}{\pi^2 a E} \left[(1-\nu)N_1(r,\theta) + \nu N_2(r,\theta) \right] F_x - \nu N_3(r,\theta) F_y$$
 (2)

$$u_y(r,\theta) = \frac{1+\nu}{\pi^2 a E} \left[-\nu N_3(r,\theta) F_x + (1-\nu) N_1(r,\theta) + \nu N_4(r,\theta) \right]$$
(3)

Here the E describes the substrate stiffness (Young's modulus) and ν the Poisson ratio. The functions N_1 to N_4 have the following form in the inner region where

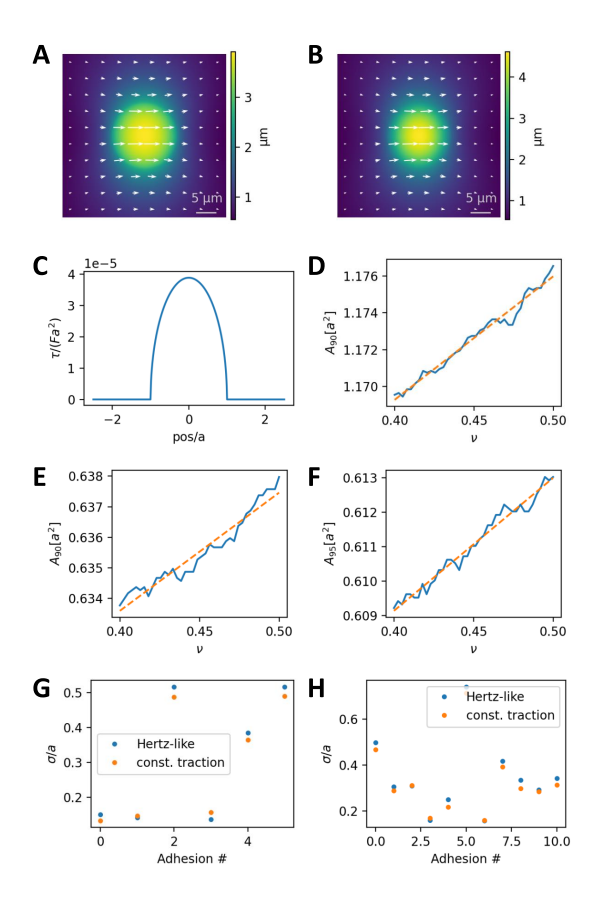


Figure 1: **A** Plot of the surface deformation created by a constant-traction profile with $a=8\,\mu\mathrm{m},\ F=\pi a^2\cdot 1.5\,\mathrm{kPa},\ E=6.9\,\mathrm{kPa},\ \nu=0.5.$ **B** Plot of the surface deformation created by a Hertz-like profile, same parameters as in A **C** cross-section for the Hertz like profile. **D** Numerical relation between between A_{90} and ν for the constant-traction profile **E** Same relation for the Hertz-like profile. **F** Numerical results relation between between A_{95} and ν for the constant-traction profile **G** Comparison of the relative standard derivation in the definition of areas for the cell presented in Fig. 5 of our main manuscript. **H** Same for the cell presented in Fig. 2 of our main manuscript.

 $r < a \text{ and } \xi_1 = r^2/a^2$:

$$N_1 = 4E_0(\xi_1) \tag{4}$$

$$N_2 = \frac{4\cos(2\theta)\left((r^2 + a^2)E_0(\xi_1) + (r^2 - a^2)K_0(\xi_1)\right)}{3r^2} + 4\sin^2\theta E_0(\xi_1)$$
 (5)

$$N_3 = \frac{2\sin(2\theta)\left((r^2 - 2a^2)E_0(\xi_1) + (r^2 - a^2)K_0(\xi_1)\right)}{3r^2}$$
(6)

$$N_4 = 4\cos^2\theta E_0(\xi_1) - \frac{4\cos(2\theta)\left((r^2 + a^2)E_0(\xi_1) + (r^2 - a^2)K_0(\xi_1)\right)}{3r^2}.$$
 (7)

Here, E_0 and K_0 describe the complete elliptic integral of the first and second kind, respectively. For the outer region where r > a and $\xi_2 a^2/r^2$ we have

$$N_1 = \frac{4\left(r^2 E_0(\xi_2) + (a^2 - r^2)K_0(\xi_2)\right)}{ar} \tag{8}$$

$$N_2 = \frac{\left(6r^2 - 2(r^2 - 2a^2)\cos(2\theta)\right)E_0(\xi_2) + 2(r^2 - a^2)(\cos(2\theta) - 3)K_0(\xi_2)}{3ar}$$
(9)

$$N_3 = \frac{2\sin(2\theta)\left((r^2 - 2a^2)E_0(\xi_2) + (a^2 - r^2)K_0(\xi_2)\right)}{3ar}$$
(10)

$$N_4 = \frac{\left(6r^2 + 2(r^2 - 2a^2)\cos(2\theta)\right)E_0(\xi_2) - 2(r^2 - R^2)(\cos(2\theta) + 3)K_0(\xi_2)}{3ar}.$$
(11)

The shape of the deformation field is shown in Fig. 1.

In the limit $r \to 0$ we find that

$$\mathbf{F} = \frac{\pi a E}{(1+\nu)(2-\nu)} \mathbf{u}(0) . \tag{12}$$

This is the relation between overall force and displacement in the middle of the focal adhesion. For the Green's function, this displacement would diverge, because it only describes the far field.

The surface deformation created by a tangential traction force distributed in a Hertz-like manner over a circular area is known from contact mechanics [3]. Employing Cartesian coordinates centered around the center of the circular adhesion, and the abbreviation $r = \sqrt{x^2 + y^2}$ the surface traction profile is given by:

$$\boldsymbol{\tau}(x,y) = \begin{cases} \frac{3\mathbf{F}}{2\pi a^3} \sqrt{a^2 - r^2} & r < a \\ 0 & r \ge a \end{cases}$$
 (13)

A linear cross-section of this deformation profile is shown in Fig. 1. The corresponding deformation field is given by:

$$u_x(x,y) = \frac{3(1+\nu)}{8Ea^3}((W_1 + W_2)F_x + W_3F_y)$$
 (14)

$$u_y(x,y) = \frac{3(1+\nu)}{8Ea^3} (W_3 F_x + (W_1 + W_4) F_y)$$
 (15)

The functions W_1 to W_4 have the following form in the inner region where r < a:

$$W_1 = \frac{1}{4}4(2-\nu)a^2 \tag{16}$$

$$W_2 = -\frac{1}{4}((4-3\nu)x^2 + (4-\nu)y^2)$$
(17)

$$W_3 = \frac{1}{4}2\nu xy\tag{18}$$

$$W_4 = -\frac{1}{4}((4-3\nu)y^2 + (4-\nu)x^2). \tag{19}$$

For the outer region where r > a and $\xi_2 = a^2/r^2$ we have:

$$W_1 = \frac{2 - \nu}{\pi} \left((2a^2 - r^2) \arcsin \frac{a}{r} + ar\sqrt{1 - \frac{a^2}{r^2}} \right)$$
 (20)

$$W_2 = \frac{\nu}{2\pi} \left(r^2 \arcsin \frac{a}{r} + (2a^2 - r^2) \frac{a}{r} \sqrt{1 - \frac{a^2}{r^2}} \right) \frac{x^2 - y^2}{r^2}$$
 (21)

$$W_3 = \frac{1}{\pi} \left(r^2 \arcsin \frac{a}{r} + (2a^2 - r^2) \frac{a}{r} \sqrt{1 - \frac{a^2}{r^2}} \right) xy \tag{22}$$

$$W_4 = \frac{\nu}{2\pi} \left(r^2 \arcsin \frac{a}{r} + (2a^2 - r^2) \frac{a}{r} \sqrt{1 - \frac{a^2}{r^2}} \right) \frac{y^2 - x^2}{r^2}.$$
 (23)

The shape of this deformation is also shown in Fig. 1.

In the limit $r \to 0$, we find, that:

$$\mathbf{F} = \frac{8aE}{3(1+\nu)(2-\nu)}\mathbf{u}(0) \ . \tag{24}$$

Compared with Eq. (12), we see that both scale linear in Young's modulus and patch size. Also the contribution related to the Poisson ratio is equivalent. They differ only in the constant prefactor.

In general, the deformation fields in both cases share many similarities. In both cases the absolute value of the deformation field $u_{abs} = \sqrt{u_x^2 + u_y^2}$ takes its maximal value at the center of the deformation. In addition the isolines of the u_{abs} field enclose simple connected regions always containing the center of the coordinate system. We define A_h to be the area where $u_{abs}(x,y) > hu_{abs}(0,0)$. While the deformation field ${\bf u}$ is dependent on five parameters $E, \ \nu, \ a, \ F_x$ and F_y , only two of them a and ν will affect A_h . Because of the way we can choose our unit scale, it can be easily seen, that a contributes quadratically $(A_h \propto a^2)$. A numerical analysis (Fig. 1) reveals that the relation to ν can be estimated using a linear function. Therefore, the expression $A_h = (y_h + m_h \nu)a^2$ describes the relationship between A_h , a and ν . The constants y_h and m_h can be determined numerically by simulating the situation for an arbitrary choice of the five parameters mentioned above. An estimation of the total force ${\bf F}$ of

an Hertz-like or constant-traction contact based on the deformation field can be found using Eq. (12) or (24), by finding the deformation at the a center of the contact. The contact radius a can be calculated from the isoline-enclosed area A_h for some value h.

The overall algorithm to determine forces \mathbf{F}_i within each adhesion now contains the following steps done individually for each adhesion search area i:

- 1. Interpolate the deformation field onto a regular spaced square grid for each time step.
- 2. Calculate the absolute value u_abs of the deformation field for each time step.
- 3. Locate the center of the adhesion by making use of the fact that u_abs should reach its maximum in this location for each time step.
- 4. A common issue in the above estimation is the fact that the adhesion in adjacent search areas might cause the center of the current adhesion not to correspond to the global maximum of u_abs within its search area, in which case the largest value for u_abs can be found right next to the adhesion search area boundary. In these cases, we rely on an interpolation from the other time-steps to select the presumed location for the area estimate.
- 5. Now that we have determined the center of the adhesion for each time step and the radius a, we can determine the deformation ${\bf u}$ in the adhesion center.
- 6. Calculate the area A_h within the adhesion search area where u_abs lies within 1-h=5%, 10%, 20%, 30% of its maximal value for each time step.
- 7. For each time step and each threshold value an estimate for the adhesion radius a can now be determined using the above mentioned area formula $a = \sqrt{A_h/(y_h + m_h \nu)}$ using the predetermined values for y_h and m_h In general, all of this estimates should yield a similar value, as the radius of the adhesion is expected not to change during the procedure.
- 8. The final estimate for the adhesion radius can now be found by finding the mean of the estimates determined in the previous step. We explicitly emit those time steps form the calculation, where we had to use the interpolation from the other time-steps in step 4, as the estimates in these cases are particularly unreliable.
- 9. Now that we have determined the deformation \mathbf{u} in the center of each adhesion for each time step and the radius a, we can determine the corresponding force \mathbf{F}_i using Eq. (12) or (24).

In order to determine whether adhesion sites can be better described by Hertz-like or the constant-traction profiles, we compare the statistic variance

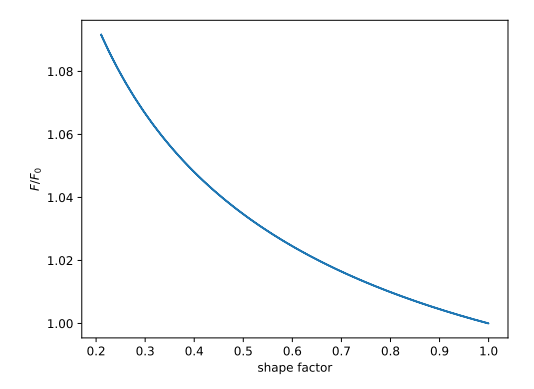


Figure 2: Ratio between the predicted force for an elliptical contact and a circular contract of equal contact area F/F_0 for $\nu = 0.5$ using Eq. (26). The horizontal axes describes the shape factor given as defined by [4].

between the radius estimates derived from different search area estimates in step 7. As can see (Fig 1. G and H) both approaches give a similarly consistent image in this regard. As the constant-force approach gives a slightly better estimate, we chose the constant traction estimate for our experimental analysis.

These two approaches assume a circular shape of the adhesion area, while many recent studies have suggested a more elliptic shape [4]. In case of a Hertz like contact, the surface traction profile can be modeled, if we assume that both the direction of the force, as well as one of the semi-axes are parallel to the x-axes:

$$\tau(x,y) = \begin{cases} \frac{3F_x \mathbf{e}_x}{2\pi a b} \sqrt{1 - \frac{x^2}{a^2} - \frac{x^2}{b^2}} & \frac{x^2}{a^2} + \frac{y^2}{b^2} < 1\\ 0 & \frac{x^2}{a^2} + \frac{y^2}{b^2} \ge 1 \end{cases}$$
(25)

The deformation field for force central displacement relation at the center is given by [5]:

$$\mathbf{F} = \frac{8\sqrt{ab}E}{3N(\nu, a/b)(2-\nu)(1+\nu)}\mathbf{u}(0) . \tag{26}$$

The function $N(\nu, a/b)$ is given by

$$N\left(\nu, \frac{a}{b}\right) = \begin{cases} \frac{4}{\pi(2-\nu)} \sqrt{\frac{a}{b}} \left(K_0(m_a) - \nu \frac{K_0(m_a) - E_0(m_a)}{m_a} \right) & a < b \\ 1 & a = b \\ \frac{4}{\pi(2-\nu)} \sqrt{\frac{b}{a}} \left((1-\nu) K_0(m_b) + \nu \frac{K_0(m_b) - E_0(m_b)}{m_b} \right) & a > b \end{cases}$$
 (27)

with the definition $m_a=1-a^2/b^2$ and $m_b=1-b^2/a^2$. Its inverse 1/N describes the ratio between the force predicted using Eq. (26) and the one predicted using Eq. (24) for a circular adhesion of equal area. In Fig. 2 1/N is plotted against the

shape factor $\frac{\pi^2}{4} \frac{b}{a} \frac{1}{E_0(m_a)^2}$. Assuming a shape factor of 0.5 as observed by [4], we see that the force increase is only around 4% which is likely below the accuracy of the prediction.

Calculation of force moments

The force monopole is the net directed force on the substrate and defined by

$$\mathbf{F} = \int \boldsymbol{\tau} d^2 x \ . \tag{28}$$

Knowing the adhesion patches, this means that we can find the total force monopole vector by simply summing up the force contributions of all adhesions:

$$\mathbf{F} = \sum_{k} \mathbf{F}_{k} \ . \tag{29}$$

Due to momentum conservation, the force monopole should be equivalent to the force transmitted by the cantilever into the cell.

We also define the first order moment matrix M as [6]

$$M_{ij} = \int x_i \tau_j d^2 x \ . \tag{30}$$

The coordinate frame for this integral is chosen with respect to the center of force of the system, which is given by

$$\boldsymbol{x}_{\mathrm{CF}} = \left(\int |\boldsymbol{\tau}| d^2 x\right)^{-1} \int |\boldsymbol{\tau}| \boldsymbol{x} d^2 x \tag{31}$$

which can be calculated in any coordinate frame.

Inserting the traction profile for patches (Eq. 13 or Eq. 1) yields:

$$\boldsymbol{x}_{\mathrm{CF}} = \left(\sum_{k} |\mathbf{F}_{k}| d^{2}x\right)^{-1} |\mathbf{F}_{k}| \boldsymbol{x}_{k} d^{2}x , \qquad (32)$$

$$M_{ij} = \sum_{k} (\boldsymbol{x}_k)_i (\mathbf{F}_k)_j d^2 x . \tag{33}$$

The diagonal components of the moment matrix describe the contractility of the system. The two off-diagonal components corresponds to a torque relative to the center of force [6]. We define the contractile momentum by

$$\mu = M_{11} + M_{22}. (34)$$

This describes the net ability to dilate or contract the cell. The net torque is defined by

$$\mathcal{M} = M_{12} - M_{21}. \tag{35}$$

Both μ and \mathcal{M} are independent of the orientation of the coordinate axes and are independent of each other.

Without needle pulling, angular momentum conservation dictates that the net torque is zero and the moment matrix symmetric. In this case, one can find an orientation of the axis such that \mathbf{M} is diagonal and the eigenvalues can be used to find the directed and isotropic contractile moment of the system. To also consider the case of needle pulling, we define a slightly modified version of the moment matrix, where we removed the torque contribution:

$$M_{ij}^{\parallel} = \int x_i x_j \frac{\boldsymbol{\tau} \cdot \boldsymbol{x}}{\boldsymbol{x}^2} d^2 x \ . \tag{36}$$

If we again insert the definition of the patches, we obtain:

$$M_{ij}^{\parallel} = \sum_{k} (\boldsymbol{x}_k)_i (\boldsymbol{x}_k)_j \frac{\mathbf{F}_k \cdot \boldsymbol{x}_k}{\boldsymbol{x}_k^2} . \tag{37}$$

This matrix is symmetric and thus an orthogonal eigendecomposition can be found. The two eigenvalues describe the dipole moments and the eigenvector corresponding to the major dipole describes the main contractile axis. This can be proven by comparing the trace of M^{\parallel} to the contractile momentum μ , which both yield the same value.

Young's modulus of PDMS-pillars used for microneedle calibration

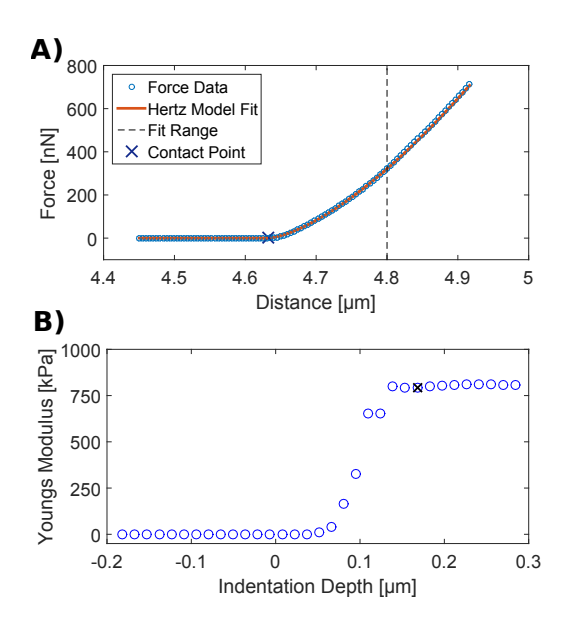


Figure 3: The Young's modulus of the PDMS pillars employed for the calibration of the microneedle was measured using an AFM indentation based method published by Huth et al. [7]. A silica bead with 21 µm diameter was glued to an AFM cantilever and was subsequently used to indent the PDMS sample with a setpoint force of 700 nN at 1 µm/s. A shows an exemplary indentation curve with a Hertz model fit. Our method employs an algorithm that calculates the Young's modulus for different indentation depths. The resulting curve is presented in **B**. The Young's modulus is determined by finding a plateau in this curve and finding the value with lowest fitting residuals. This value is marked in **B** with a black cross. The sample was indented 16 times at each of 32 different positions resulting in a mean value of 801.49 +/-32.91 kPa.

Young's modulus of the polyacrylamide sample

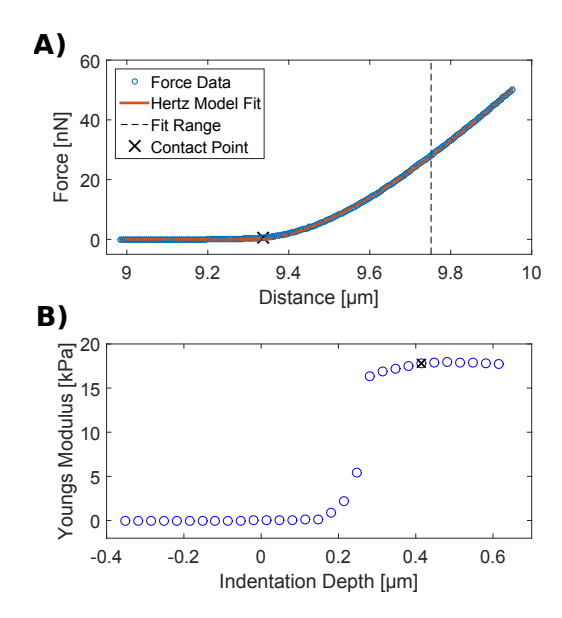


Figure 4: The Young's modulus of a polyacrylamide (PAAm) sample that serves as a traction force microscopy substrate needs to be known in order to calculate traction forces from the displacement of the beads embedded in the sample. We employed the same method to measure the Young's modulus of our PAAm samples as for the PDMS pillars. Indentation curves were collected at a cantilever speed of 1 μ m/s and a setpoint force of 50 nN. **A** shows an exemplary indentation curve with a Hertz model fit, while **B** shows the resulting Young's modulus versus indentation depth. The sample was indented 16 times at each of 30 different positions resulting in a mean value of 16.49 + -0.55 kPa.

Traction forces in perpendicular direction

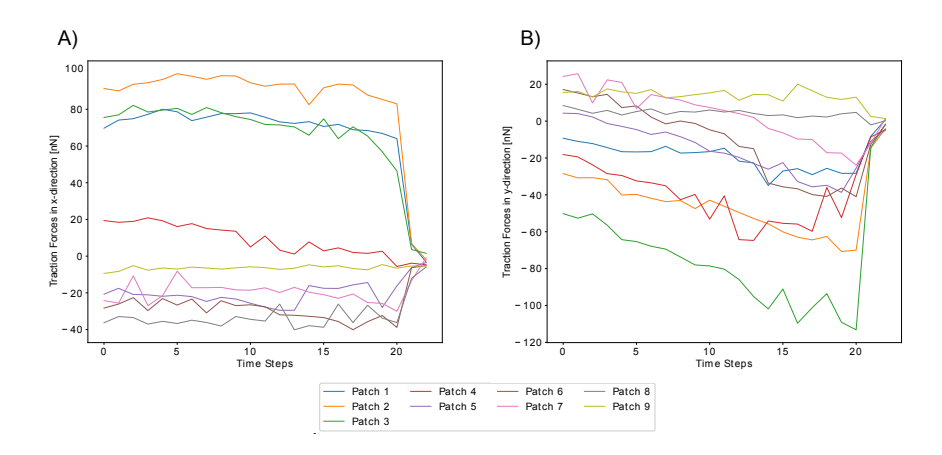


Figure 5: Traction force data from the cell presented in Fig. 2 of our main manuscript. **A** shows the x-components of the traction force vectors. It is very clear the these are not influenced by the shearing in y-direction, which is why we focus our discussion on traction forces in y direction. **B** shows the y-components of the traction forces for each adhesion patch. We decided to combine some neighbouring patches with similar behavior for better visualization. We combined patches 2,3 and 4 as well as 5,6 and 7.

References

- U.S. Schwarz, N.Q. Balaban, D. Riveline, A. Bershadsky, B. Geiger, and S.A. Safran. Calculation of forces at focal adhesions from elastic substrate data: The effect of localized force and the need for regularization. *Biophysical Journal*, 83(3):1380–1394, 2002.
- [2] Yunfei Huang, Christoph Schell, Tobias B Huber, Ahmet Nihat Şimşek, Nils Hersch, Rudolf Merkel, Gerhard Gompper, and Benedikt Sabass. Traction force microscopy with optimized regularization and automated Bayesian parameter selection for comparing cells. *Scientific Reports*, 9(1):539, 2019.
- [3] Kenneth L. Johnson. Contact Mechanics. Cambridge University Press, 1985.
- [4] Dong-Hwee Kim and Denis Wirtz. Focal adhesion size uniquely predicts cell migration. *The FASEB Journal*, 27(4):1351–1361, 2013.
- P. J. Vermeulen and K. L. Johnson. Contact of nonspherical elastic bodies transmitting tangential forces. *Journal of Applied Mechanics*, 31(2):338–340, June 1964.

- [6] James P. Butler, Iva Marija Tolić-Nørrelykke, Ben Fabry, and Jeffrey J. Fredberg. Traction fields, moments, and strain energy that cells exert on their surroundings. *American Journal of Physiology-Cell Physiology*, 282(3):C595–C605, March 2002.
- [7] Steven Huth, Sandra Sindt, and Christine Selhuber-Unkel. Automated analysis of soft hydrogel microindentation: Impact of various indentation parameters on the measurement of Young's modulus. *PLoS ONE*, 14(8):e0220281, 2019.